Available online at www.sciencedirect.com
SCIENCE DIRECT®
PERGAMON
International Journal of Heat and Mass Transfer 46 (2003) 4657–4667
International Journal of HEAT and MASS TRANSFER
www.elsevier.com/locate/ijhmt

An impingement cooling on a flat surface by using circular jet with longitudinal swirling strips

Mao-Yu Wen *, Kuen-Jang Jang

Department of Mechanical Engineering, Cheng-Shiu Institute of Technology, Kaohsiung 833, Taiwan, ROC

Received 14 August 2002; received in revised form 21 May 2003

Abstract

This work presents and discusses the results of an experimental investigation of the heat transfer between the constant-heat-flux test plate and the impinging jets. The round jets with/without swirling inserts are used. Smoke flow visualization is also used to investigate the behavior of the complicated flow phenomena under the swirling-flow jet for this impingement cooling. The effects of flow Reynolds numbers ($500 \leqslant Re \leqslant 27,000$), the geometry of the nozzle (BR, LSS and CSS), and jet-to-test plate placement ($3 \leqslant H/d \leqslant 16$) are examined.

1. Introduction

The continuing increase of power densities in electronic packages and the simultaneous drive to the reduction of size and weight of electronic products have led to the use of air cooled heat sinks by applying impinging, rather than parallel, flow to the channel. Impinging jets have been used in a variety of applications such as cooling of hot steel plates, cooling of turbine blades, drying of textiles, and cooling of electronic equipment. Jet impingement is an effective means of localized heating or cooling. Along with the recently developed techniques such as phase-change and jet impingement cooling, forced air cooling will also continue to be used in the technology of the future because it is inexpensive and robust.

Yang et al. [1] presented the heat transfer results of jet impingement cooling on a semi-circular concave surface and clearly explained the significant effects of the nozzle geometry and the curvature of the plate. A wide variety of nozzles was tested by Garimella and Nenaydykh [2], and Colucci and Viskanta [3] to determine the effect of the nozzle geometry on local convective heat transfer rate for jet impingement cooling on a flat plate. Gauntner et al. [4] presented a review report of the flow characteristics of a turbulent jet impinging on a flat plate. Martin [5] carried out heat and mass transfer studies on impinging jets and presented results which are based on experimental data for single round nozzle, arrays of round nozzles, single slot nozzle, and arrays of slot nozzles.

Hwang and Cheng [6] utilized a transient liquid crystal technique to evaluate the detailed heat transfer coefficients on two principal walls of a triangular duct with a swirling flow. Three different angle between the swirling jet and the duct axial direction were examined. Remarkable results were obtained. The wall-averaged Nusselt number for the bottom and target walls of the triangular duct was insensitive to different jet inlet angles. Algifri and Bhardwaj [7] carried out an analytical study of heat transfer characteristics in decaying turbulent swirling flow in a pipe. Heat transfer was predicted by assuming a rotating slug flow, which was the case for the swirling flow generated by a shot-twisted tape. Ward and Mahmood [8] presented mass and heat transfer rates associated with orthogonal impingement of single, swirling, air jets onto flat plates. Mass transfer data were determined using a thin-film naphthalene sublimation technique and a Chilton–Colburn analogy was employed to infer the corresponding heat transfer coefficients. Very little

* Corresponding author. Tel./fax: +886-7-733-7100.
E-mail address: wmy@cc.csit.edu.tw (M.-Y. Wen).

0017-9310/$ - see front matter © 2003 Elsevier Ltd. All rights reserved.
doi:10.1016/S0017-9310(03)00302-8

Nomenclature

A	surface area of the test plate (m^2)
a	sectional area of the swirling-strip insert (m^2)
A_f	flow area of the tube, $(\pi d^2/4) - a$ (m^2)
b	thickness of stainless steel foil (m)
d	inner diameter of the tube (m)
D_h	hydraulic diameter of the tube with swirling-strip insert, A_f/p (m)
H	jet-to-plate distance (m)
h	local convective heat transfer coefficient defined in Eq. (4) ($W m^{-2} K^{-1}$)
I	electrical current (A)
k	thermal conductivity of fluid ($W m^{-1} K^{-1}$)
k_s	thermal conductivity of the stainless steel foil ($W m^{-1} K^{-1}$)
L	length of the jet (m)
Nu	local Nusselt number defined in Eq. (5)
$\overline{Nu}$	average Nusselt number defined in Eq. (6)
Nu_0	Nusselt number at stagnation point
Pr	Prandtl number
P	the wetted perimeter (m)
q_g	generated heat flux ($W m^{-2}$)
q_{loss}	heat loss ($W m^{-2}$)
q_w	convective heat flux ($W m^{-2}$)
R	effectiveness evaluation criterion, constant pumping power
Re	jet Reynolds number, $4\dot{V}/\pi v D_h$
T_{aw}	adiabatic wall temperature (K)
T_i	temperature at inner bed of the heater (K)
T_j	air temperature at jet exit (K)
T_j^*	heated jet temperature (K)
T_w	wall temperature (K)
u	average velocity of air in the jet, $\dot{V}/A_f$ ($m s^{-1}$)
V	voltage drop across the surface (V)
$\dot{V}$	volumetric flow rate, uA_f ($m^3 s^{-1}$)
r	radial distance from stagnation point (m)
z	axial length of the tube (m)

Greek symbols

δ	strip thickness (m)
$\cos\phi$	power factor
v	kinematic viscosity of air ($m^2 s^{-1}$)
ρ	density ($kg m^{-3}$)

Subscripts

BR	tube without any insert
CSS	crossed-swirling-strip insert
fl	full-length inserts
insert	with insert
LSS	longitudinal swirling-strip insert
no	without insert
T	length refers to the jet

work has been reported on flow field visualization of either the circular conventional impinging jets or swirling impinging jets. Flow visualization studies on a turbulent large-scale flow structure for a free plane jet flow were conducted by [9]. Salce and Simon [10] also visualized the swirl flow of air inside a cylindrical cavity using the smoke wires technique. The images of the flow field, however, did not show the whole flow field.

Most of the above studies of jet impingement cooling mainly focused on a circular tube without/with either decaying or continuous swirling flow and on a flat plate. The impingement cooling on a flat surface by using jet issuing through longitudinal swirling strips have not been performed. In the present investigation, the heat transfer from a flat surface to an impinging air jet is examined as a function of nozzle exit-to plate distance, and Reynolds number. The jet issued from a tube without/with two different inserts (swirling-strip type inserts: longitudinal swirling-strip (LSS), and crossed-swirling-strip (CSS)). Turbulence structures of the impinging jet over a flat surface are also studied by flow visualization.

2. Description of experiment

2.1. Experimental apparatus

A schematic representation of the test setup is shown in Fig. 1. Air supplied from a blower system passes through a heat exchanger, a shut-off valve, a filter, a flow meter and a settling chamber before entering the circular tube. The tube was made of copper. It had an internal diameter of 7 mm, a wall thickness of 1.0 mm, and a length of 250 mm. In addition, in order to impart swirl to the jet, the tube had different longitudinal swirling strip inserts as shown in Fig. 2. The swirling strip was made of 1.5 mm thick copper strips, the width of the strip being 0.1 mm more than the inside diameter of the tube. The strips were twisted on a lathe by manual rotation of the chuck. There was interference fit between the tube and the swirling strip insert. The length of the tube was selected in such a way as to ensure that the length-to-diameter ratios ($=25.8$) was larger than that needed for the air flow at the exit of the tube to reach fully developed status [11]. The total air flow rate was controlled by an inverter.

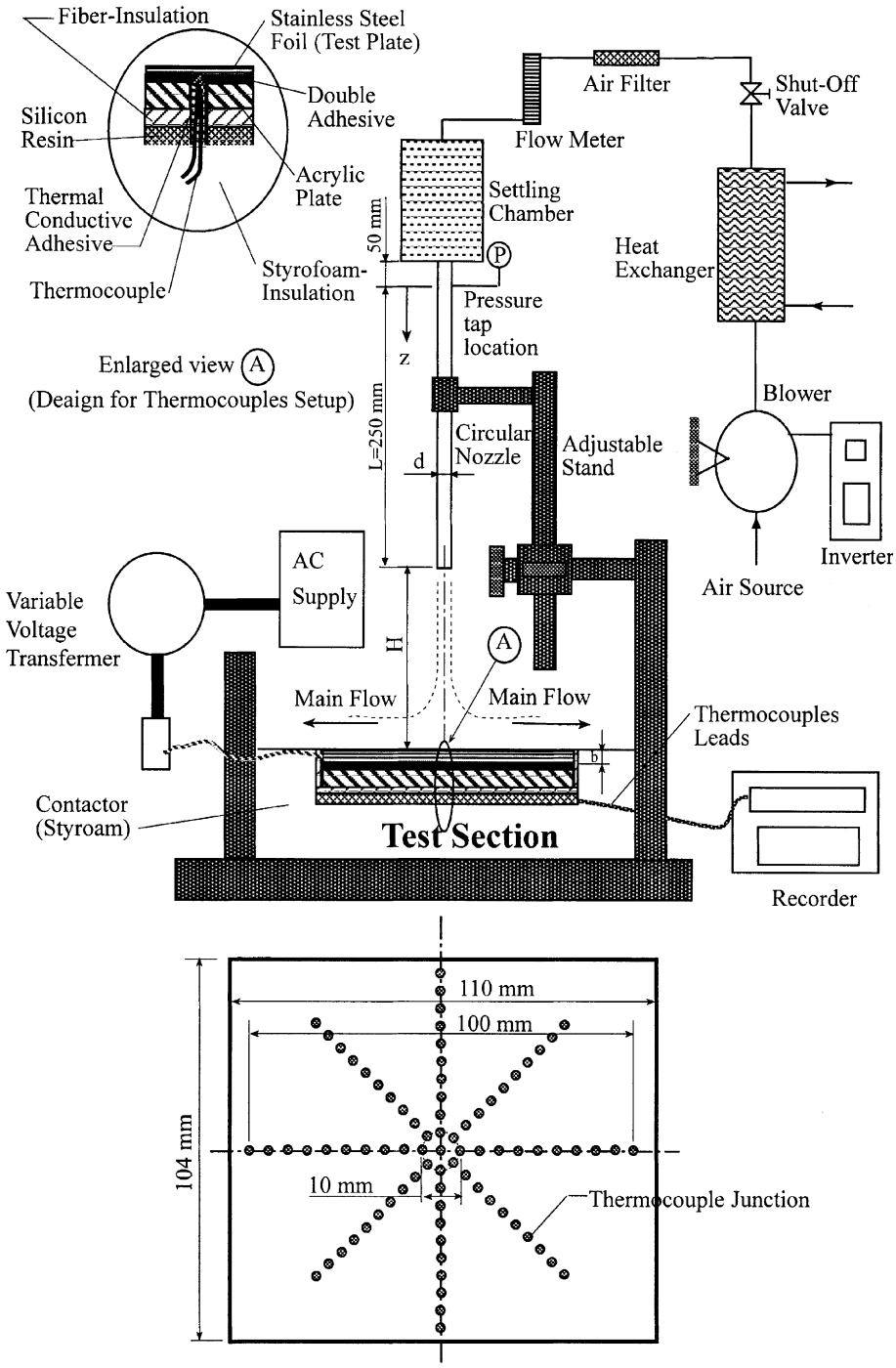

Fig. 1. A schematic of experimental setup and thermocouple arrangement.

The heat exchanger was installed to obtain the constant temperature flow at the nozzle exit and to reduce the temperature difference between the ambient air and the air nozzle exit within ±0.2 °C. A uniform and stable flow distribution was established at the tube exit using a settling chamber of 450×450×500 mm in volume.

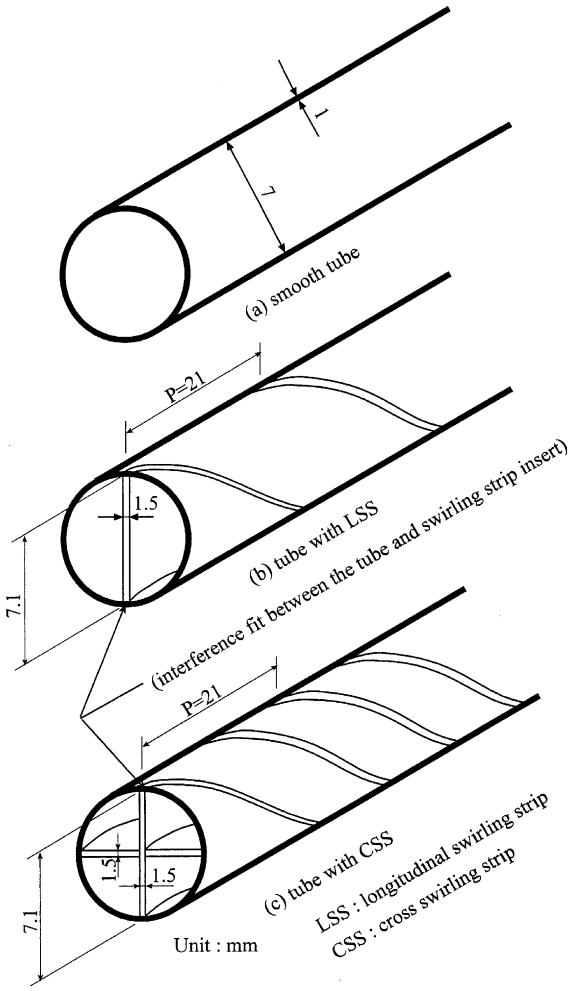

Fig. 2. Experimental apparatus for nozzle geometry.

Air rotameters were used to measure the air volumetric flow rate ($\dot{V}$). (It is measured by one of three flow meters depending on the range), which was corrected using the measured air temperature and pressure after exiting the flow meters. The pressure tap located on the tube wall is used to measure pressure drop. Pressure drop was measured by means of vertical U-tube manometer with dibutyl phthalate and mercury as the manometric fluid for lower Re and higher Re, respectively. (The jet support frame was used to adjust the elevation, H of the jet from the heated surface and to maintain the jet in the vertical position. The surface temperature along the cooled surface was measured under constant heat flux condition. The surface was made of a stainless steel foil (104×110 mm). To ensure that the stainless steel foil was maintained at a constant heat flux, the strip was heated with a high power AC source passing through a thin (0.05 mm thick) stainless steel foil. With the desired voltage (V) controlled by a variable voltage transformer and current (I) measured by both the current transformer and the power meter passing through the thin strip, the heat flux along the surface could be calculated. The thin stainless steel foil was bonded to the outer surface of the acrylic plate by double-side adhesive tape. Thermocouples were attached to the foil (thermal contact resistance $=0.042\times10^{-4}$ m^2 K/W) and three issued from an inner acrylic surface through drilled holes, and the void space was completely filled with thermal epoxy. The inner acrylic surface was backed by a fiber-insulation board of low thermal conductivity ($=0.038$ W/m K) in order to minimize the heat loss through the bottom and sides of the test plate. The temperature of the back surface of the test plate was measured using 36-gage (0.13 mm diameter wire) copper–constantan thermocouples installed at equal distance. In addition to the thermocouple placed at the center of the test section to measure the foil temperature at the stagnation point, there were a total of 20 thermocouples in each direction (see Fig. 1). Calibrated copper–constantan thermocouples were used to measure the temperature of the back surface of the test plate. The data were logged by a recorder (180 mm Hybrid recorder, AH3000, chino). A detailed cross-sectional view of the thermocouples setup designed for more accurate temperature measurements is shown in Fig. 1.

2.2. Data reduction and uncertainty

The heat flux, q_g in the heating foil was controlled by the variation of output voltage and this was calculated by measuring the voltage drop (V) between the voltage taps soldered in the heating foil, the electrical current (I) and the power factor ($\cos\phi$). The convective heat flux (q_w) was calculated as follows:

$$q_w = q_g - q_{loss} \approx \frac{VI\cos\phi}{A}, \tag{1}$$

where A is the area of the test plate (a heated foil). The term q_{loss} is a small correction for conduction and radiation losses from the element. The correction never exceeded 3% of q_g in the present study. By performing a detailed analysis, the maximum possible errors are individually obtained as follows: (1) radiation loss: 0.1% (2) non-uniformity of the heating foil: 1.8% (3) lateral solid heat conduction: 0.5% and (4) heat loss through insulation: 0.4%. The wall temperature T_w at the outer surface of the heater can be calculated by one-dimensional heat conduction model at each applied heat flux (q_w) as

$$T_w = T_i - \frac{q_w b}{k_s}. \tag{2}$$

The Reynolds number is defined as $Re = uD_h/v$ where u is the velocity of the air leaving the tube, D_h is the hydraulic diameter, and v is the kinematic viscosity of air. Putting $\dot{V} = uA_f$ we have

$$Re = 4\dot{V}/\pi v D_h. \quad (3)$$

The effects of jet entrainment temperature on heat transfer have been investigated by [12–15]. The heat transfer coefficient is defined in terms of the difference between the heated wall temperature and the adiabatic wall temperature and it is independent of the temperature difference between the jet and the ambient. Therefore, it is possible to use heat transfer data for an unheated jet ($T_j^* = T_j$) for the heated jet if the effectiveness is known and the local heat transfer coefficient is defined in terms of the adiabatic wall temperature. The local heat transfer coefficient based on the difference between the wall temperature and adiabatic wall temperature is well established [16,17]. The local heat transfer coefficient is defined as

$$h = \frac{q_w}{T_w - T_{aw}}, \quad (4)$$

the adiabatic wall temperature ($T_{aw} = T_i$) distribution is measured at the inner surface of test plate based on zero wall-heat flux. Approximately 0.5 h is required to reach steady-state condition for each test run. Experimental results for heat transfer are presented in terms of the Nusselt number

$$Nu = \frac{hD_h}{k}. \quad (5)$$

The uncertainty analysis was performed by using methods suggested by [18] with 95% confidence level. The maximum uncertainties in measurement were estimated at: heat flux ±1.7%, heat transfer coefficient ±6.2%, Nusselt number ±6.5%, Reynolds number ±3.0% and friction factor ±5.1%.

3. Results and discussion

Three cases were run with a jet impinging normal to the flat plate. One case had an open tube (BR), one had a longitudinal swirling strip insert (LSS), and one a cross swirling strip insert (CSS). The experiments were conducted at 10 different Reynolds number (250, 500, 750, 1000, 2100, 4400, 9300, 16,500, 21,000 and 27,000) for jet-to-plate spacings (H/d) of 3, 5, 8, 12 and 16).

3.1. Flow visualization

The smoke generated by a smoke generator is injected into the plenum before the blower is turned on. Flow visualization experiments were conducted using the same jet assembly as in the heat transfer experiments, a strong light resource, a black background, and a camcorder and a 35 mm camera to record images of the flow fields. The smoke flow technique was used to show images of the complete flow field, both between the jet exit and the impinged surface, and horizontally along the impinged surface, up to 35 mm from the stagnation point. The flow visualization showed how swirls affected the flow field and induced mixing on the impinged surface. Fig. 3(a)–(c) show the flow fields of BR, LSS, and CSS at $Re = 500$. In general, the impinging flow structures of the impinging jet before arriving at the wall observed for the round jet with LSS/CSS are significantly different from that of the round jet without any insert. The flow fields of CSS (Fig. 3(c)) showed four distinct radial flow streams exiting the housing tube and continuing to about 1.5 jet diameter from jet exit before combining to form a flow cone similar to that of BR (Fig. 3(a)), but with a larger diameter at the top due to higher entrainment of ambient air (Fig. 3(b)–(c)). The spiral channels formed by the LSS/CSS introduced swirling flow components in the jet flow, causing it to spread radially outward after exiting the housing tube. The radial spread of the flow of the present study increased as the narrow channels in the housing tube widened (Fig. 3(b and c). The heat transfer on impinged surface was the highest at the radial location where the jet flow cone impinged the surface. Outside and inside the flow cone, flow mixing and hence heat transfer rate was lower.

Fig. 4 shows photographs of the entire flow field induced by BR, LSS, CSS at $H/d = 3$–12 and $Re = 4400$. In general, in Fig. 4(a)–(c), these patterns

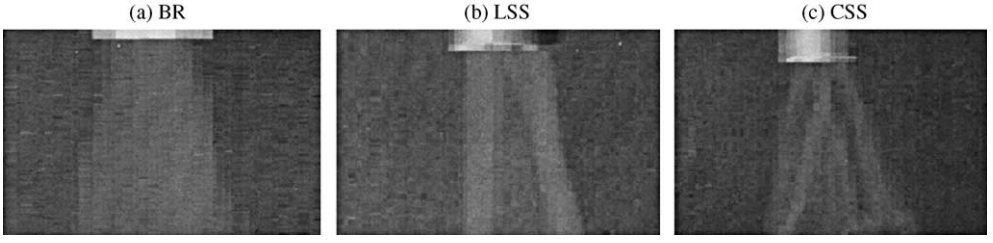

Fig. 3. Comparison of flow field among the BR, LSS and CSS at $Re = 500$.

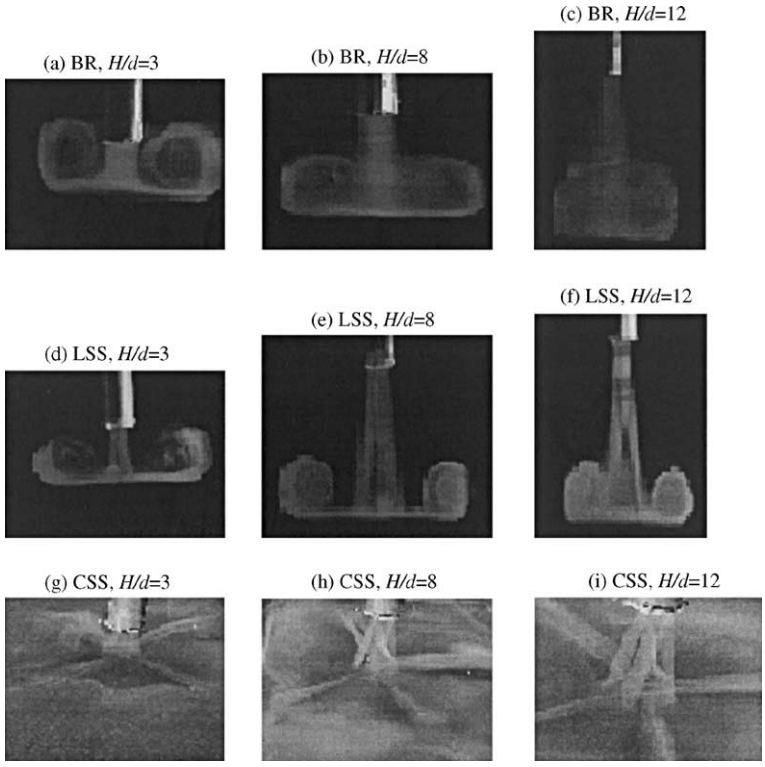

Fig. 4. Photographs of flow field for different nozzle types and jet-to-plate distances at $Re = 4400$.

have the symmetric vortex cells. Also, as the H/d increases, it was found that the strength of the symmetric vortices decreases. In addition, the flow field in the region extending from the exit of the tube to about one and half jet diameter from it was basically a parallel flow and the flow gradually changed to a triangular cone as it approached the impinged surface due to the entrainment of surrounding air. The minor diameter of the BR flow cone was about one jet diameter, d, while its major diameter on the impinged surface was $\sim 2d$. As a result, the strength of the turbulence in the case of the BR on the impinged surface was the highest at the centerline of the jet (or at the stagnation point), and it became gradually weaker radially outward from the stagnation point. The air flow impinging the surface developed into a parallel boundary layer along the surface, which subsequently formed vortices, some radial distance apart from the stagnation point. These vortices moved radially outward with the decrease in jet spacing or increase in Reynolds number (not shown here). Similarly, a pair of symmetric vortex cells for the LSS is observed in Fig. 4(d)–(f). Taking a closer view, the impinging flow structures of the impinging jet after arriving at the wall observed for the LSS (Fig. 4(d)–(f) are significantly different from those of the BR (Fig. 4(a)–(c)). However, the vortices shown in Fig. 4(d)–(f) are yawed. This is because the yawed vortices were formed due to the complex interaction among centrifugal force, buoyancy force and the special swirling flow streams where air impinged the surface. The complicated yawed flow phenomenon persisted until the flow spread horizontally along the impinged surface up to 35 mm in radial diameter. Fig. 4(g)–(i) gave very clear images of the complete flow field for the present case of CSS; it showed how swirls affected the flow field and induced mixing on the impinged surface. It also indicated that CSS seems to have a stronger turbulence, and the degree of turbulence decreased with increasing H/d. However, the images of the flow fields for the BR, LSS and CSS shown in Fig. 4 confirmed the measured radial distributions of Nu in heat transfer experiments, showing local Nusselt number peaking at or near the stagnation point and then decreasing exponentially with increasing radial distance from the stagnation point. When the jet-to-plate distances increased, the jet flow fields shaped like a pyramid (Fig. 4(e, f), and (h, i)). The spiral flow dominated up to a vertical distance of about three jet diameters from the exit of the housing tube. Below that, the flow spread widely in the radial direction, impinging the surface over a larger distance from the stagnation point than the BR with the same nozzle-to-plate distance.

3.2. Heat transfer coefficient

The local Nusselt number distribution along the plate is shown in Fig. 5 for different nozzle types (BR, LSS and CSS) and three jet Reynolds numbers (4400, 16,500 and 27,000). Common to all results ($500 \leqslant Re \leqslant 2700$) is the trend of monotonic increase in Nu with increasing Re. Also, Nu decreased with increasing radial distance from its maximum value at (for BR) and near (for LSS and CSS) the stagnation point. For the range of Re from 500 to 27,000 the gradual reduction in the Nu continues beyond $r/d > 1.0$. Furthermore, this result clearly demonstrated that both the LSS and CSS markedly enhanced heat transfer rate on the impinged surface compared to BR at same Re and H/d. However, Nu values for the CSS were much higher than those for LSS and BR, particularly at and near the stagnation point. It was found that Nu had a saddle-shaped radial distribution, which was symmetric about the center line of the jet ($r = 0$), similar to that of [19]. As Re increased, the difference between peak Nu and that at the stagnation point increased, decreasing the radial uniformity of Nu in the vicinity of stagnation point. It is worth noting that BR always produced a more uniform radial distribution of Nu than LSS and CSS, but Ma [20], and Ward and Mahamood [8] reported the swirling jets provided a more uniform radial distribution of local impingement jets than normal impingement. This reverse result seems due to the different definition of the jet Reynolds number (based on the mean nozzle exit velocity in the non-swirling case, not the definition in the present paper). Based on the present definition of the Reynolds number, the swirling jets have the small Re than that of the above Refs. [8,20] under the fixed pumping power. Moreover, the effect of jet spacing H/d on Nu is also much more significant for CSS than LSS and BR where as Nu for all jets decreased as H/d increased (see Fig. 6).

Fig. 7 shows the stagnation point Nusselt number (Nu_0) versus nozzle-to-plate distance (H/d) for three

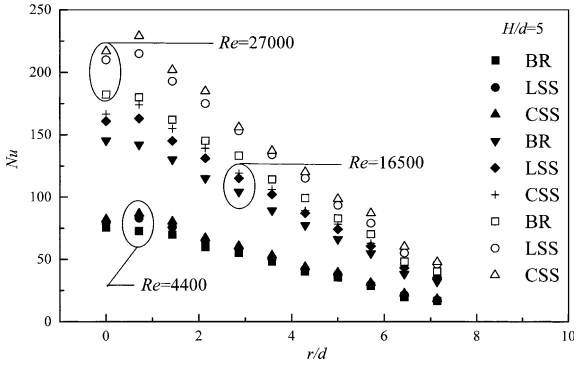

Fig. 5. Measured radial Nusselt number distribution at different Re and for different nozzle types.

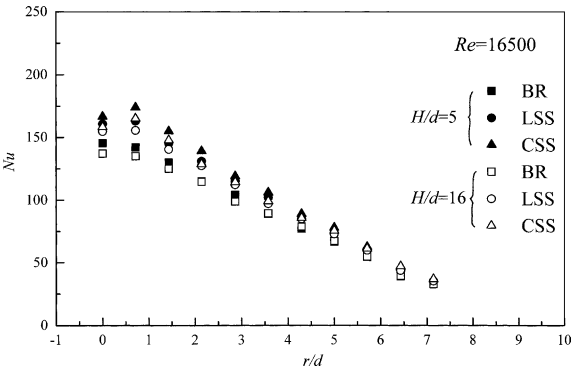

Fig. 6. Measured radial Nusselt number distribution for different nozzle types and at different H/d.

different nozzles. The plot shows that, the increasing centerline turbulence with increasing Re results in an increasing Nusselt number (Nu_0). Moreover, no perceptible dependence of Nu_0 on H/d was detected. The results under present study are in good agreement with the previous results [21,22]. The percentage increase in the stagnation point Nusselt number for the cases of round jet with different inserts (LSS and CSS) were found to vary up to 6%, but in most of cases the increase was about 4–5%.

Using numerical integration the average Nusselt number ($\overline{Nu}$) is given by Eq. (6) as follows:

$$\overline{Nu} = \frac{2}{r^2}\int_0^r r \cdot Nu \, dr. \tag{6}$$

The effect of jet-to-plate distance on the average Nusselt number for different nozzles and Re is shown in Fig. 8. In general, the average Nusselt number ($\overline{Nu}$) increases rapidly with decreasing H/d at $H/d < 8$ and with increasing Re. When H/d is greater than 8, the variation of $\overline{Nu}$ is generally much smaller, and the variation among the present BR, LSS and CSS is not

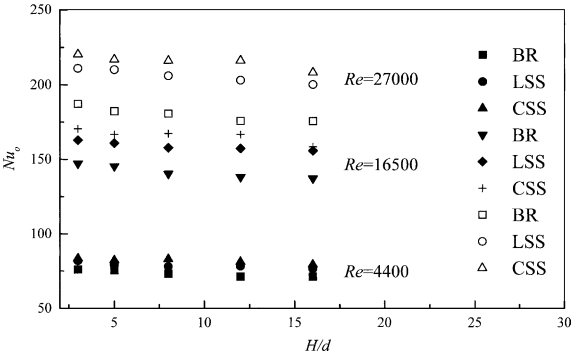

Fig. 7. Stagnation point Nusselt number versus H/d for different nozzles.

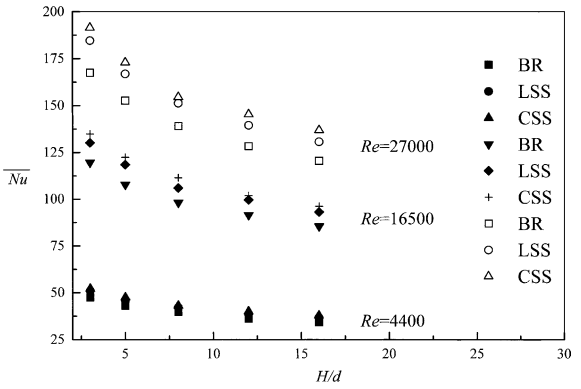

Fig. 8. Effect of nozzle-to-plate distances on the average Nusselt number for different nozzles.

noticeable for low Re. However, it suggests that lower H/d has a higher $\overline{Nu}$, the highest $\overline{Nu}$ is for CSS and this is followed by LSS and BR. The present study also shows that an increase in the average Nusselt number for the round jet with two different inserts is more pronounced around the tip of the potential core of the circular jet (not shown here). This increase can be attributed to more vigorous mixing in case of the round jet with swirling-strip type insert.

3.3. Correlations of Nusselt number

Considering now the effects of different nozzles on the stagnation point Nusselt number with respect to Reynolds number, the present Nusselt number at the stagnation point plotted against the Reynolds number is shown in Fig. 9. Generally speaking, the effects of H/d on stagnation point Nusselt number shown in Fig. 8 seems insignificant (the variation of Nu_0 versus H/d is less than 5% (see Fig. 7)). However, it was found that the Nu_0 increases mainly due to increase in Re. The Prandtl number term (Pr) will be familiar from other established correlation ($Pr^{1/3}$). Since this value (1/3) is commonly used to express the effect of change in Pr in jet-impingement systems [8]. However, the exponent of 2/5 instead of 1/3 was also used, the reason has been discussed both [5,20]. Although the Pr of present study was limited, its effect is well known and is, therefore, included for completeness. This indicates that there exists a plot like Fig. 9 for the correlations of stagnation Nusselt number versus Reynolds number for different nozzles. The correlation predicts 98% of point within ±25% and 85% of points within ±10%. For round jet without any insert, the Nusselt number in the stagnation point coincides with the laminar stagnation theory [23], which yields the dependence $Nu_0 \propto Re^{0.5}$. Furthermore, it is noted by Hollworth and Gero [24] that appreciable deviations from the theory may occur in the stagnation region due to the effects of turbulence in the jet freestream. However, for the present round jet with different inserts, the Reynolds number dependence is stronger ($Nu_0 \propto Re^{0.520}$ for present LSS and $Nu_0 \propto Re^{0.533}$ for present CSS). This is attributed to the increase of turbulence intensity in the present jet with inserts as a result of the stronger exchange of momentum with the surrounding ambient air. This behavior agrees closely with the results of Pan et al. [25]. The correlations recommended by Zheng et al. [26] and by Webb and Ma [27] for the large Pr number were much higher and much lower than that of the present study, respectively. These differences seem due to the different Pr number and the different jets. But, as predicated by Zheng et al. [26] and by Webb and Ma [27], the Nu_0 data shown the same dependence (the trend) on Re as does the present BR case. In addition, the correlation developed by Tawfek [28] for $7240 \leqslant Re \ll 27{,}000$, $H/d = 16$ and $d = 7$ mm, agrees with the present results with the average difference of less than 9% for BR case. However, the agreement is weakened at higher Reynolds number (for $Re > 27{,}000$) with a maximum difference of more than 16%.

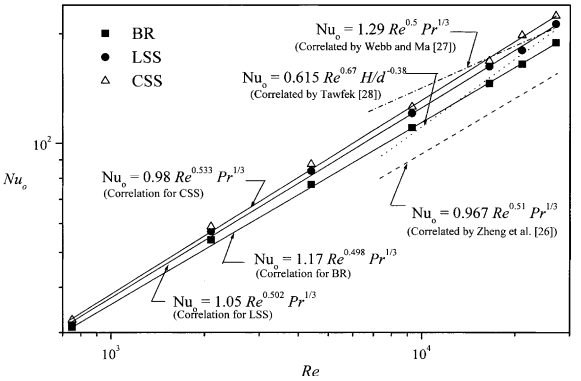

Fig. 9. Variation of the stagnation point Nusselt number with Reynolds number for different nozzles.

Fig. 10 shows the correlations of the average Nusselt number versus Reynolds number for different nozzles. Similar to Hrycak [29] and Tawfek [28] ($\overline{Nu} \propto Re^{0.7}$), the calculated values of $\overline{Nu}$ were found to be best correlated in terms of $Re^{0.696}$, $Re^{0.702}$ and $Re^{0.706}$ for the present BR, LSS and CSS, respectively. However, $\overline{Nu}$ was strong functions of H/d, r/d (see Figs. 6 and 8) and Pr. The results are satisfactorily correlated as

$$\overline{Nu} = 0.442 Re^{0.696} Pr^{1/3} (H/d)^{-0.20} (r/d)^{-0.41} \quad \text{for present BR,} \tag{7}$$

$$\overline{Nu} = 0.452 Re^{0.702} Pr^{1/3} (H/d)^{-0.20} (r/d)^{-0.41} \quad \text{for present LSS,} \tag{8}$$

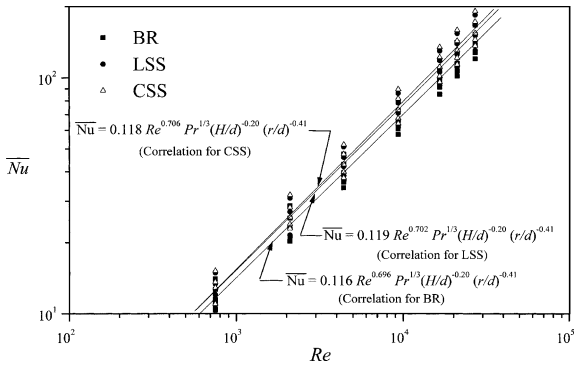

Fig. 10. Variation of the average Nusselt number with Reynolds number for different nozzles.

$$\overline{Nu} = 0.448 Re^{0.706} Pr^{1/3} (H/d)^{-0.20} (r/d)^{-0.41} \quad \text{for present CSS,} \tag{9}$$

in the range $3 \leqslant H/d \leqslant 16$, $0 \leqslant r/d \leqslant 7.14$ and $750 \leqslant Re \leqslant 27,000$. The maximum deviation of the above correlations and the average Nusselt numbers obtained from the experimental data is less than ±10%.

3.4. Performance evaluation

Of special interest for studies of impingement heat transfer augmentation for the round jet with LSS/CSS is the question of how much the heat transfer is increased relative to a round jet without any insert (BR) at the same condition. The impingement heat transfer of the present round jet with/without inserts (LSS, CSS/BR) may be predicted, as in the cases from Eqs. (8) and (9), using an auxiliary factor from Fig. 11 for different nozzles. The performance evaluation for the present geometry with swirling insert has been evaluated *a* on the criterion of increase in heat duty at constant pumping power as suggested by [30]. The performance ratio, R is given by

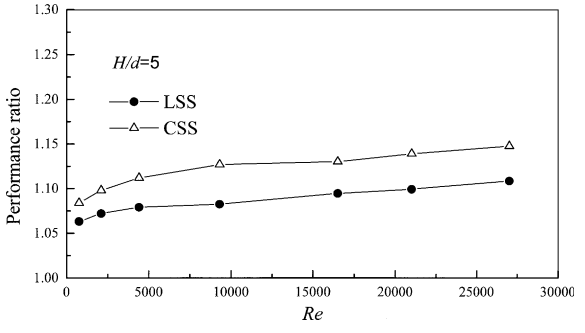

Fig. 11. Performance ratio with Reynolds number for different nozzles.

$$R = \frac{(\overline{Nu})_{\text{insert}}}{(\overline{Nu})_{\text{fl}}}, \tag{10}$$

where the subscripts "insert" and "fl" stand for a partial insert and full-length insert, respectively. $(\overline{Nu})_{\text{fl}}$ at a given Reynolds number, Re_{fl} is estimated for equal pumping power in smooth with insert, and calculated by the following

$$Re_{\text{insert}} = \left[\left(\frac{f_{\text{fl}}}{f_{\text{f,insert}}}\right)\left(\frac{A_{\text{f,fl}}}{A_{\text{f,insert}}}\right)\right]^{1/3} Re_{\text{fl}}, \tag{11}$$

$$A_{\text{f,fl}} = \frac{\pi d^2}{4}, \tag{12}$$

$$A_{\text{f,LSS}} = \left[\left(\frac{\pi d^2}{4} - \delta d\right)L + \frac{\pi d^2}{4}(L_{\text{T}} - L)\right] \Big/ L_{\text{T}}, \tag{13}$$

$$A_{\text{f,CSS}} = \left[\left(\frac{\pi d^2}{4} - 2\delta d + \delta^2\right)L + \frac{\pi d^2}{4}(L_{\text{T}} - L)\right] \Big/ L_{\text{T}}. \tag{14}$$

The $f_{\text{f,insert}}$ versus $Re_{\text{f,insert}}$ curves were consulted and trial and error method was adopted.

Fig. 11 shows the performance ratio at $H/d = 5$ for the cases of present LSS and CSS. It shows that CSS has the better heat transfer performance than that of LSS. The percentage increase in the heat transfer enhancement was found to vary up to 9% and 14% for the case of the present cases of LSS and CSS, respectively. In general, the enhancement ratios in both cases (LSS and CSS) are increased as the Reynolds number increased. Moreover, no significant effect of the H/d on the enhancement factor has been found (see Fig. 7). Taking a closer view, for lower Reynolds number ($Re \leqslant 5000$), it was found that there is a rapid increase in performance ratio for both LSS and CSS as Re increases. This is because the flow yields the secondary vortex with rapid increase in both size and strength in the flow pattern at early stage ($Re \leqslant 5000$).

4. Conclusions

Heat transfer and flow visualization experiments were performed to investigate and compare the heat transfer performance of the swirling jets (LSS and CSS) with that of a conventional impinging jet (BR) having the same tube diameter at the same conditions. The experiments were performed for a fixed jet diameter ($d = 7$ mm) and the constant-heat-flux test plate (stainless steel foil). Reynolds number was varied from 500 to 27,000 and the jet-to-plate distance (H/d) was also varied in the range of 3 and 16. The principal conclusions are derived as follows.

1. The flow visualizations brought about a good understanding of the flow field: air flow development after exiting the jet housing tube, flow mixing and formation of vortices on the impinged surface and entrainment of ambient air.
2. The local as well as the average heat transfer was strong function of r/d, Re and H/d, but no perceptible dependence of Nu_0 on H/d was detected. The percentage increase in the stagnation point Nusselt number for the cases of round jet with different inserts was found to vary up to 6%, but the increase was mostly about 4–5%. However, it suggests that lower H/d has a higher $\overline{Nu}$ the highest $\overline{Nu}$ is for CSS and this is followed by LSS and BR, respectively.
3. The heat transfer rate increases as the jet spacing decreases owing to the reduction in the impingement surface area.
4. Simple correlations of the stagnation point Nusselt number (Nu_0) as well as the average Nusselt number ($\overline{Nu}$) have been derived for all the nozzle types and other pertinent variables. These correlations provide useful information for potential industrial applications.
5. The performance analysis has shown that CSS has the better heat transfer performance than that of LSS. The percentage increase in the heat transfer enhancement was found to vary up to 9% and 14% for the case of the present LSS and CSS, respectively. The performance ratios of both LSS and CSS increase as the Reynolds number increases.

Acknowledgements

This research was sponsored by the Cheng-shiu Institute of Technology of Taiwan under contract no. CSIT-91-53.

References

[1] G. Yang, M. Chio, J.S. Lee, An experimental study of slot jet impingement cooling on concave surface: effect of nozzle configuration and curvature, Int. J. Heat Mass Transfer 42 (1999) 2199–2209.
[2] B. Garimella, B. Nenaydykh, Nozzle-geometry effects in liquid jet impingement heat transfer, Int. J. Heat Mass Transfer 39 (1996) 2915–2923.
[3] D.W. Colucci, R. Viskanta, Effect of nozzle geometry on local convective heat transfer to a confined impinging air jet, Exp. Thermal Fluid Sci. 13 (1996) 71–80.
[4] J.W. Gauntner, J.N.B. Livingwood, P. Hrycak, Survey of literature on flow characteristics of a single turbulent jet impinging on a flat plate, NASA TN D-5652, 1970.
[5] H. Martin, Heat and mass transfer between impinging gas jets and solid surfaces, in: Advances in Heat Transfer, vol. 13, Academic Press, New York, 1997, pp. 1–60.
[6] J.-J. Hwang, C.-S. Cheng, Augmented heat transfer in a triangular duct by using multiple swirling jets, ASME J. Heat Transfer 121 (1999) 683–690.
[7] A.H. Algifri, R.K. Bhardwaj, Prediction of the heat transfer for decaying turbulent swirl flow in a tube, Int. J. Heat Mass Transfer 28 (1985) 1637–1647.
[8] J. Ward, H. Mahamood, Heat transfer from a turbulent swirling, impingement jets, in: Proceedings of the Seventh International Heat Transfer Conference, 1982, pp. 401–408.
[9] D.J. Shlien, A.K.M.F. Hussain, Visualization of the large-scale motion of a plane jet, flow visualization, in: Proceedings of the Third International Symposium of Flow Visualization, 1983.
[10] A. Salce, T.W. Simon, Investigation of the effects of flow swirl on heat transfer inside a cylindrical cavity, ASME J. Heat Transfer 113 (5) (1991).
[11] W.M. Rohsenow, J.P. Hartnett, E.N. Ganic, Hand-Book of Heat Transfer Application, McGraw-Hill, New York, 1985.
[12] S.A. Striegl, T.E. Diller, An analysis of the effect of entrainment temperature on jet impingement heat transfer, ASME J. Heat Transfer 106 (1984) 804–810.
[13] B.R. Hollworth, L.R. Gero, Entrainment effects on impingement heat transfer. Part II: local heat transfer measurements, ASME J. Heat Transfer 107 (1985) 910–915.
[14] R.J. Goldstein, K.A. Sobolik, W.S. Seol, Effect of entrainment on the heat transfer to a heated circular air jet impinging on a flat surface, ASME J. Heat Transfer 112 (1990) 608–611.
[15] J.W. Baughn, T.E. Hechanova, X. Yan, An experimental study on entrainment effects on the heat transfer from a flat surface to a heated circular impinging jet, ASME J. Heat Transfer 113 (1991) 1023–1025.
[16] E.M. Sparrow, R.J. Goldstein, M.A. Rouf, Effect of nozzle surface separation distance on impingement heat transfer for a jet in a crossflow, ASME J. Heat Transfer 97 (1975) 528–533.
[17] R.J. Goldstein, A.I. Behbahani, Impingement of a circular jet with and without cross flow, Int. J. Heat Mass Transfer 25 (1982) 1377–1382.
[18] S.J. Kline, F.A. McClintock, Describing uncertainties in single sample experiments, Mech. Eng. 75 (1953) 3–8.
[19] K.N. Agafonov, Heat transfer in a turbulent twisted jet incident on a plane barrier, Heat Transfer Sov. Res. 23 (1991) 378–383.
[20] C.F. Ma, Impingement heat transfer with meso-scale fluid jets, in: Proceedings of 12th International Heat Transfer Conference, 2002.
[21] T. Nakatogawa, N. Nishiwaki, M. Hirata, K. Tofii, Heat transfer of round turbulent jet impinging normally on flat plate, in: Proceedings of 4th International Heat Transfer Conference, FC 5.2, 1970.
[22] F. Giralt, C. Chia, O. Trass, Characterization of the impingement region in and axisymmetric turbulent jet, Ind. Eng. Chem. Fundamentals 16 (1997) 21–28.
[23] Y. Katto, Introduction to Heat Transfer, Yokendo, Tokyo, 1970, pp. 68–72, (in Japanese).
[24] B.R. Hollworth, L.R. Gero, Entrainment effects on impingement heat transfer: Part II—local heat transfer measurements, ASME J. Heat Transfer 107 (1985) 910–915.

[25] Y. Pan, J. Stevens, B.W. Webb, Effect of nozzle configuration on transport in the stagnation zone of axisymmetric, impinging free surface liquid jets: Part 2—local heat transfer, ASME J. Heat Transfer 114 (1992) 880–886.
[26] Q. Zheng, C.F. Ma, Y. Zhuang, D.H. Lei, Local characteristics of recovery factor and heat transfer coefficient with impinging free-surface jets of large *Pr* number liquid, J. Eng. Thermophys. 18 (1997) 217–220.
[27] B.W. Webb, C.F. Ma, Single-phase liquid jet impingement heat transfer, Adv. Heat Transfer 26 (1995) 105–217.
[28] A.A. Tawfek, Heat transfer and pressure distributions of an impinging jet on a flat surface, Heat Mass Transfer 32 (1996) 49–54.
[29] P. Hrycak, Heat transfer from round impinging jets to a flat plate, Int. J. Heat Mass Transfer 26 (1983) 1857–1865.
[30] A.E. Bergles, A.R. Blumenkrantz, J. Taborek, Performance evaluation criterion for enhanced heat transfer surfaces, in: Proceedings of the International Heat Mass Transfer Conference, vol. 2, 1974, pp. 239–243.